University of Groningen

Experimental and numerical investigation of the origin of surface roughness in laser powder bed fused overhang regions

Feng, Shaochuan; Kamat, Amar M.; Sabooni, Soheil; Pei, Yutao T.

Published in:
Virtual and Physical Prototyping

DOI:
10.1080/17452759.2021.1896970

IMPORTANT NOTE: You are advised to consult the publisher's version (publisher's PDF) if you wish to cite from it. Please check the document version below.

Document Version
Publisher's PDF, also known as Version of record

Publication date:
2021

Link to publication in University of Groningen/UMCG research database

Citation for published version (APA):
Feng, S., Kamat, A. M., Sabooni, S., & Pei, Y. T. (2021). Experimental and numerical investigation of the origin of surface roughness in laser powder bed fused overhang regions. *Virtual and Physical Prototyping*, *16*(sup. 1), S66-S84. https://doi.org/10.1080/17452759.2021.1896970

Copyright
Other than for strictly personal use, it is not permitted to download or to forward/distribute the text or part of it without the consent of the author(s) and/or copyright holder(s), unless the work is under an open content license (like Creative Commons).

The publication may also be distributed here under the terms of Article 25fa of the Dutch Copyright Act, indicated by the "Taverne" license. More information can be found on the University of Groningen website: https://www.rug.nl/library/open-access/self-archiving-pure/taverne-amendment.

Take-down policy
If you believe that this document breaches copyright please contact us providing details, and we will remove access to the work immediately and investigate your claim.

Downloaded from the University of Groningen/UMCG research database (Pure): http://www.rug.nl/research/portal. For technical reasons the number of authors shown on this cover page is limited to 10 maximum.

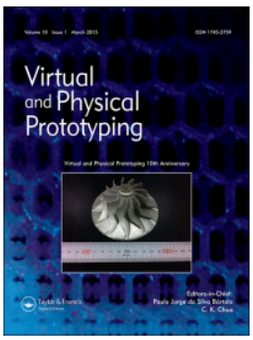

Virtual and Physical Prototyping

ISSN: (Print) (Online) Journal homepage: https://www.tandfonline.com/loi/nvpp20

Experimental and numerical investigation of the origin of surface roughness in laser powder bed fused overhang regions

Shaochuan Feng, Amar M. Kamat, Soheil Sabooni & Yutao Pei

To cite this article: Shaochuan Feng, Amar M. Kamat, Soheil Sabooni & Yutao Pei (2021) Experimental and numerical investigation of the origin of surface roughness in laser powder bed fused overhang regions, Virtual and Physical Prototyping, 16:sup1, S66-S84, DOI: 10.1080/17452759.2021.1896970

To link to this article: https://doi.org/10.1080/17452759.2021.1896970

© 2021 The Author(s). Published by Informa UK Limited, trading as Taylor & Francis Group

Published online: 10 Mar 2021.

Submit your article to this journal

Article views: 908

View related articles

View Crossmark data

Full Terms & Conditions of access and use can be found at
https://www.tandfonline.com/action/journalInformation?journalCode=nvpp20

VIRTUAL AND PHYSICAL PROTOTYPING
2021, VOL. 16, NO. S1, S66–S84
https://doi.org/10.1080/17452759.2021.1896970

Taylor & Francis
Taylor & Francis Group

OPEN ACCESS Check for updates

Experimental and numerical investigation of the origin of surface roughness in laser powder bed fused overhang regions

Shaochuan Feng [a,b], Amar M. Kamat [a], Soheil Sabooni[a] and Yutao Pei [a]

[a]Department of Advanced Production Engineering, Engineering and Technology Institute Groningen, Faculty of Science and Engineering, University of Groningen, Groningen, the Netherlands; [b]School of Mechanical Engineering, University of Science and Technology Beijing, Beijing, People's Republic of China

ABSTRACT

Surface roughness of laser powder bed fusion (L-PBF) printed overhang regions is a major contributor to deteriorated shape accuracy/surface quality. This study investigates the mechanisms behind the evolution of surface roughness (R_a) in overhang regions. The evolution of surface morphology is the result of a combination of border track contour, powder adhesion, warp deformation, and dross formation, which is strongly related to the overhang angle (θ). When $0° \leq \theta \leq 15°$, the overhang angle does not affect R_a significantly since only a small area of the melt pool boundaries contacts the powder bed resulting in slight powder adhesion. When $15° < \theta \leq 50°$, powder adhesion is enhanced by the melt pool sinking and the increased contact area between the melt pool boundary and powder bed. When $\theta > 50°$, large waviness of the overhang contour, adhesion of powder clusters, severe warp deformation and dross formation increase R_a sharply.

ARTICLE HISTORY
Received 18 January 2021
Accepted 25 February 2021

KEYWORDS
Laser powder bed fusion (L-PBF); melt pool dynamics; overhang region; shape deviation; surface roughness

1. Introduction

Laser powder bed fusion (L-PBF) is an advanced additive manufacturing (AM) technique wherein metal powder is selectively fused using a focused laser beam to build up a three dimensional (3D) metallic part layer by layer according to sliced 3D computer-aided design (CAD) models (Chatham, Long, and Williams 2019; Tan, Zhu, and Zhou 2020). Depending upon whether material exists below the printed layer or not, the printed region can be classified as either a solid region or an overhang region, respectively. An overhang region is thus a special structure that is built not on a solid substrate but rather directly on top of the powder bed (Patterson, Messimer, and Farrington 2017). Overhang regions can be built with or without support structures, and the L-PBF of overhang regions with supports is similar to the process on a solid substrate (Wang and Chou 2018) with the exception that the supports are built with lower density (and hence lower mechanical strength) than solid substrates, making it easier to mechanically remove them after the L-PBF process. Overhang regions printed with support structures thus need additional post-processing steps, namely support removal, grinding, and polishing after the L-PBF process.

In some particular cases such as the fabrication of horizontal interior channels, the overhang region in the top half of the channels has to be built without supports because of the difficulties of removing the supports after the process (Hopkinson and Dickens 2000). In addition to support structures not being possible for horizontal internal channels, it is also difficult to implement any surface finishing processes in the internal surfaces, especially for complex 3D channel networks encountered in conformal cooling channels (Feng, Kamat, and Pei 2021). As a result, the overhang region can deviate from its designed shape owing to: (i) residual stress-induced deformation, (ii) staircase effect (Kuo et al. 2020; Li et al. 2020), and (iii) enhanced surface roughness caused by undesired powder sintering; where, the former two factors are classified into 'macro' deviations usually in the mm length scale and the latter one is recognised as 'micro' deviation usually in the μm length scale.

Thermal stress-induced deformation is an important problem encountered in overhang regions (Patterson, Messimer, and Farrington 2017). The local melting/cooling induces large temperature gradients in and around the melt pool causing intensive thermal stresses

CONTACT Shaochuan Feng shaochuan.feng@rug.nl, fengshaochuan@ustb.edu.cn Department of Advanced Production Engineering, Engineering and Technology Institute Groningen, Faculty of Science and Engineering, University of Groningen, Nijenborgh 4, Groningen 9747 AG, the Netherlands; School of Mechanical Engineering, University of Science and Technology Beijing, Beijing 100083, People's Republic of China

© 2021 The Author(s). Published by Informa UK Limited, trading as Taylor & Francis Group
This is an Open Access article distributed under the terms of the Creative Commons Attribution License (http://creativecommons.org/licenses/by/4.0/), which permits unrestricted use, distribution, and reproduction in any medium, provided the original work is properly cited.

in the solidified layers. Thermal stress-induced warping does not deform the solid regions appreciably since these regions are constrained by many layers below; on the other hand, the overhang regions are unconstrained and suffer significant deflection due to stress relief during the process (Kamat and Pei 2019). Moreover, the melt depth is larger than the layer thickness (since previous layers are also remelted to ensure sufficient bonding between the built layers [Yadroitsev et al. 2013; Kamath et al. 2014]), which induces a shape deviation (such as dross [Charles et al. 2020; Feng et al. 2020]) since the solidified thickness is larger than the designed one. In the microscale, printed surfaces (R_a and $S_a \sim 10$ μm) are rougher than mechanically machined surfaces (Duval-Chaneac et al. 2018; Wen et al. 2018). This problem is especially severe for overhang regions whose surface roughness (R_a) is usually around 20 μm as a result of unmelted powder adhering to the edges of the solidified melt pool (Mazur et al. 2016; Pakkanen et al. 2016).

The overhang angle (θ, measured with respect to the build direction) is a crucial parameter that affects the warp deflection of overhang regions as well as the surface roughness (Kamat and Pei 2019; Mingear et al. 2019). An overhang angle of $\theta \sim 45°$ is generally agreed upon as the critical value up to which overhang regions can be printed without support structures (Pakkanen et al. 2016; Kadirgama et al. 2018). When θ is larger than this critical value, the overhang regions cannot be printed with acceptable surface quality. Besides the overhang angle, laser parameters (related to laser energy density) also influence the surface roughness of the overhang regions by affecting the shape/size of the melt pool as well as the melt pool dynamics (Wang et al. 2013; Mingear et al. 2019).

Melt pool dynamics is a common physical phenomenon in laser materials processing, including the L-PBF processes, conducted on both the solid (Shrestha and Chou 2018) and overhang (Le et al. 2020) regions. The melt pool shape, size, and cooling rates affect both the residual stress-induced deformation as well as the surface roughness, thus acting as a bridge between processing parameters and surface morphology/quality and meriting further investigation using numerical simulations to understand the melt pool behaviour and its effect on surface roughness. To date, several studies have been conducted to simulate the melt pool behaviour during L-PBF of solid regions. Simulation techniques such as finite element method (FEM) (Roberts et al. 2009; Du et al. 2019), finite difference method (FDM) (Wu et al. 2018), computational fluid dynamics (CFD) (Lee and Zhang 2016), and arbitrary Lagrangian-Eulerian method (ALE) (Khairallah and Anderson 2014) were employed to study the heat transfer (temperature field) and mass transfer (melt flow) processes with the inclusion of evaporation recoil pressure (Hu et al. 2018) and Marangoni convection (Zhang et al. 2018) phenomena. Further, the discrete element method (DEM) was used to create a random-distributed powder bed (Lee and Zhang 2016; Wu et al. 2018). These models simulated the L-PBF processes from the powder-scale (Khairallah et al. 2016) to mesoscale (Khairallah and Anderson 2014), and from single-track (Leitz et al. 2017) to multi-track (Foroozmehr et al. 2016) and multi-layer (Huang, Khamesee, and Toyserkani 2019).

However, the melt pool dynamics in overhang regions which dictates the resulting surface roughness has received scant attention in the literature. Although existing simulation models for L-PBF of solid regions can serve as a reference to some extent, there are considerable differences in the melt pool dynamics between the overhang regions and solid regions. In overhang regions, the molten metal flows downwards into the gaps between powder particles, making the melt pool sink under the weak support offered by the porous powder bed. This makes the effects of gravity and surface tension important in the determination of the resulting shape/size of the melt pool and, subsequently, the evolution of the microscale morphology of overhang regions. Moreover, due to the voids between powder particles, thermal conditions (such as energy absorption, energy loss, cooling rate, and thermal conductivity) of printing on a powder bed are inferior to printing on a solid substrate, worsening the surface quality, porosity, and metallurgical strength of the resulting part (Yu et al. 2019; Karimi et al. 2020; Sing and Yeong 2020). Surface roughness not only increases the (micro-) shape deviation but also deteriorates the mechanical strength by serving as initiation sites for micro-cracks during periodic loading (Günther et al. 2018). The high surface roughness of overhang regions limits the application of L-PBF in the fabrication of parts that have strict requirements on (micro-) accuracy/quality.

The present study systematically and comprehensively investigates the formation mechanisms of micro shape deviation of overhang regions (built without supports) and the origins of surface roughness using experimental and simulation studies. A coupled DEM-CFD simulation model is developed to reveal the melt pool dynamics of the overhang region and formation mechanisms of surface morphology, taking into account the effects of border track contour, powder adhesion and warp deformation. The surface roughness R_a is studied as a function of overhang angle using simulations and single-factor L-PBF printing experiments. Three

mechanisms of powder adhesion in the overhang regions associated with the sinking of the melt pool are identified and discussed in detail. Finally, potential solutions to mitigate high surface roughness issue in as-printed overhang regions are discussed briefly.

2. Experimental methodology

2.1. Experimental setup and materials

The SLM 125HL machine (SLM Solutions, Germany) was used to conduct the L-PBF experiments. A random-polarized Gaussian beam ($M^2 \sim 1.19$) was produced by a fibre laser with a wavelength of 1070 nm and a focused beam diameter of 70 µm. The processing was conducted in a protective argon (Ar) atmosphere (overpressure 17 mbar). Spherical powder of 17-4 PH stainless steel (LPW Technology, UK) with a size distribution in the range of 10–45 µm was used as the experimental material in the present study. The manufacturer-specified chemical composition of the alloy is listed in Table 1.

2.2. Experimental design

2.2.1. Printing of overhang region with varying overhang angles

The shape and size of the L-PBF printed samples are illustrated in Figure 1. The samples had an overhang region with $\theta = 0°$, 15°, 30°, 45°, 50°, 55°, and 60°, respectively. The overhang regions for all the samples had the same length of 12 mm (except for the 0° cubic sample which had a 12 mm-tall vertical wall). Attempts to print overhang regions with θ greater than 60° were also made but failed during printing due to large tip warpage in the overhang region. The process parameters for the solid region (both interior and border) and overhang region (border only) were selected, as listed in Table 2, according to the recommendation of the manufacturer, which were optimised to minimise porosity in the printed samples. The solidified layer thickness was 30 µm and the build plate was preheated to 100°C during the L-PBF process.

Each layer was double contoured (i.e. an inner border and an outer border with an 80 µm spacing between the inner and outer borders). The borders in an overhang region are classified into three situations depending on the overhang angle: two solid borders ($\theta \leq 30°$), one solid border (inner) and one overhang border (outer) ($30° < \theta \leq 50°$), and two overhang borders ($\theta > 50°$), as shown in Figure 2. The printing sequence was as follows: outer border of the solid region, inner border of the solid region, the inner border of the overhang region (if applicable), outer border of the overhang region (if applicable), and finally the interior solid region.

The surface micro-morphology as well as the surface roughness in the overhang region was measured using an Alicona optical 3D measurement system (InfiniteFocus G5 plus) wherein the vertical resolution was 0.1 µm under 10× magnification. The measurement of surface roughness was conducted using the methodology of ISO 4288 ("Geometrical Product Specifications (GPS) — Surface Texture: Profile Method — Rules and Procedures for the Assessment of Surface Texture (ISO 4288)" 1996). In this standard, the roughness sampling length is recommended as 8 mm when $R_a > 10$ µm. Three points on each sample (Locations A, B, and C in Figure 1, corresponding to three distances from the start point of the overhang: 5, 6, and 7 mm, respectively) were selected to measure the surface roughness. Linear measurement was performed along two orthogonal directions (Directions I and II in Figure 1) at each measuring location. Cross-sectional micrographs are important in observing the microstructures and roughness profiles (Cai et al. 2019, 2020, 2021). Micrographs of the cross-sectional overhang regions were obtained with optical microscopy to illustrate the mechanisms of powder adhesion. The samples were mounted into a resin embedding, ground, and polished to the final step with 1 µm diamond before the optical microscopy.

2.2.2. Single-track printing

To verify the fidelity of the simulation model, single-track printing was conducted on a 17-4 PH stainless steel substrate. The experiments were conducted under the same process parameters as the printing of interior solid region (listed in Table 2) except for hatch spacing and scanning strategies that are not applicable for single-track printing. The transverse cross-section of the printed sample was ground, polished, and etched to reveal the melt pool boundary. The profile of the track contour was then observed and measured using a scanning electron microscope (SEM). The results will be presented in Section 3, where experimental and simulation-predicted melt pool dimensions will be compared.

Table 1. Chemical composition of 17-4 PH stainless steel powder*.

Element	Fe	C	Cr	Cu	Mn	Mo	N	Nb + Ta	Ni	O	P	S	Si
wt%	Bal.	0.01	15.6	3.89	0.24	<0.01	0.01	0.33	4.03	0.05	0.004	0.003	0.29

* Data from the powder supplier.

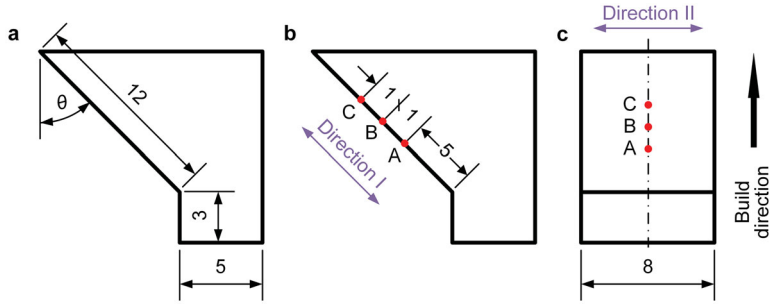

Figure 1. Shape and size of the L-PBF printed samples: (a and b) front view, (c) left view (unit: mm; overhang angle $\theta = 0°$, 15°, 30°, 45°, 50°, 55° and 60°, respectively; Points A, B and C and Directions I and II refer to the locations and directions of measuring surface roughness R_a).

Table 2. Manufacturer-recommended process parameters used in the experiments.

Parameter	Solid region		Overhang region
	Interior	Border	Border
Laser power (W)	200	100	100
Scan speed (mm/s)	800	400	1000
Hatch spacing (μm)	120	N/A	N/A
Scan strategy	Stripes, 10 mm wide	N/A	N/A
Hatch rotation angle	33° after each layer	N/A	N/A

2.2.3. Single-factor experiments for laser power and scan speed

To find out the potential solutions of high surface roughness issue in L-PBF printed overhang regions, the effects of laser power and scan speed on the surface roughness of the overhang region were studied using single-factor experiments. Samples with 45° overhang angle were built under five levels of laser power (70, 85, 100, 115, and 130 W) and five levels of scan speed (700, 850, 1000, 1150 and 1300 mm/s), where the power and scan speed refer to the overhang border parameters. The solid parameters and other overhang border parameters (except for laser power and scan speed) were maintained constant according to the manufacturer-recommended values listed in Table 2.

3. Simulation details

A coupled DEM-CFD model was developed to simulate the melt pool behaviour and predict the shape/size of the melt pool and solidified track contour. A powder bed with randomly generated particle sizes (within the range of 10–45 μm) and locations was created using

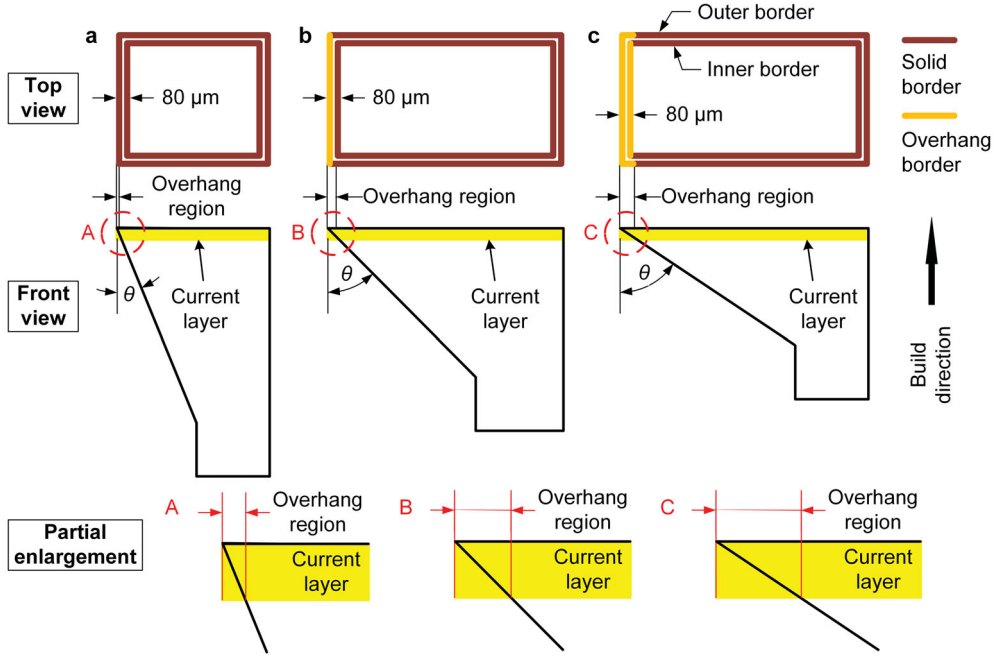

Figure 2. Borders in the overhang region depending on the overhang angle θ: (a) two solid borders when $\theta \leq 30°$, (b) one solid border and one overhang border when $30° < \theta \leq 50°$ and (c) two overhang borders when $\theta > 50°$.

Yade (Šmilauer et al. 2015), an open-source DEM software. Due to the voids between powder particles, the apparent density of the powder bed was much lower than the density of a bulk solid. This resulted in powder bed shrinkage during the printing process, causing the thickness of the solidified layer to be smaller than the thickness of the original powder bed (Li et al. 2018; Tan et al. 2019). The solidified layer thickness was around 0.5 times the thickness of the powder bed layer according to our simulation results and the experimental results in the literature (Yadroitsev et al. 2013). Therefore, to obtain a 30 µm-thick solidified layer (which remains consistent with the experimental value), the thickness of the powder bed layer was selected as 60 µm. To import the geometry model of powder bed into the CFD model, the meshing data was saved into a binary STL file.

The L-PBF process was modelled using a commercial CFD software (FLOW-3D, USA). The modelling space was meshed by cubic cells having a size of $4 \times 4 \times 4$ µm. To save computational time and cost, only a small geometry where the track was printed was modelled, not the whole substrate and powder layer. For the purpose of modelling, the model geometry was constrained by 'virtual' boundaries. Heat transfer at the boundaries was continuous and smooth, and the boundary conditions were therefore set as semi-infinite (Hu et al. 2019). The edges of the melt pool were set as free-slip wall boundaries, where the normal component of the fluid velocity field was equal to zero while the tangential component was unrestricted. The molten metal was assumed to be an incompressible fluid to which a static pressure condition was applied. The physical phenomena occurring during the L-PBF process, such as heat transfer, vaporisation, constant pressure bubbles, air entrainment, temperature-dependent surface tension (driving Marangoni convection and capillary effect in the melt pool), viscous flow and gravity, and solidification with shrinkage and microporosity, were considered in the simulation. The momentum and continuity equations were solved numerically (*Flow-3D V11.2 Documentation* 2016):

Mass continuity equation

$$\partial(uA_x)/\partial x + \partial(vA_y)/\partial y + \partial(wA_z)/\partial z = R_{SOR}/\rho \quad (1)$$

Momentum equations

$$\frac{\partial u}{\partial t} + \frac{1}{V_F}\left(uA_x\frac{\partial u}{\partial x} + vA_y\frac{\partial u}{\partial y} + wA_z\frac{\partial u}{\partial z}\right) = -\frac{\partial p}{\rho\partial x} + G_x + f_x \quad (2)$$

$$\frac{\partial v}{\partial t} + \frac{1}{V_F}\left(uA_x\frac{\partial v}{\partial x} + vA_y\frac{\partial v}{\partial y} + wA_z\frac{\partial v}{\partial z}\right) = -\frac{\partial p}{\rho\partial y} + G_y + f_y \quad (3)$$

$$\frac{\partial w}{\partial t} + \frac{1}{V_F}\left(uA_x\frac{\partial w}{\partial x} + vA_y\frac{\partial w}{\partial y} + wA_z\frac{\partial w}{\partial z}\right) = -\frac{\partial p}{\rho\partial z} + G_z + f_z \quad (4)$$

where t is time; ρ is the molten metal density; (u, v, w) are velocity components in the coordinate directions (x, y, z); (A_x, A_y, A_z) are the fractional area open to flow in the (x, y, z) directions; R_{SOR} is a mass source; V_F is the fractional volume open to flow; p is the pressure; (G_x, G_y, G_z) are body accelerations, and (f_x, f_y, f_z) are viscous accelerations. Both explicit solvers and implicit solvers were employed to solve the equations wherein explicit solvers were used for the physics of free surface pressure, viscous stress, and advection (first-order) and implicit solvers were used for the physics of heat transfer and surface tension pressure. The dynamic time step (between 10^{-8}–10^{-7} s) was automatically chosen during the simulation. An HP Z6 G4 workstation configured with a 28-core CPU (2.00 GHz frequency) and 64 GB DDR3 memory was used to perform the simulations. The material properties used in the simulations are listed in Table 3.

In laser materials processing, the laser beam irradiates the substrate and penetrates it till a certain depth. For a Gaussian laser beam, the 3D volumetric laser energy source can be conveniently approximated to be in the shape resembling an circular paraboloid inside the substrate (Figure 3a), where the base diameter is equal to the laser beam spot diameter (70 µm in our case) and the height (representing the optical penetration depth of laser beam) is related to the energy attenuation inside the powder bed. The 3D shape of the volumetric

Table 3. Material properties used in the simulations*.

Properties	Value
Density (kg/m^3)	Solid: 7260, liquid: 7249
Specific heat (J/kg K)	Solid: 722, liquid: 726
Thermal conductivity (W/m K)	Solid: 29.35, liquid: 28.95
Liquidus temperature (K)	1697.15
Solidus temperature (K)	1674.15
Vaporisation temperature (K)	3080
Volumetric thermal expansion (1/K)	1.73×10^{-5}
Surface tension (N/m)	$1.8225–4.226 \times 10^{-4}$ $(T - 1774)$
Latent heat of fusion (J/kg)	2.6×10^5
Latent heat of vaporisation (J/kg)	6.8×10^6
Convective heat transfer coefficient** (W/m^2 K)	100

* Data from Flow-3D material database. ** from powder surface to voids.

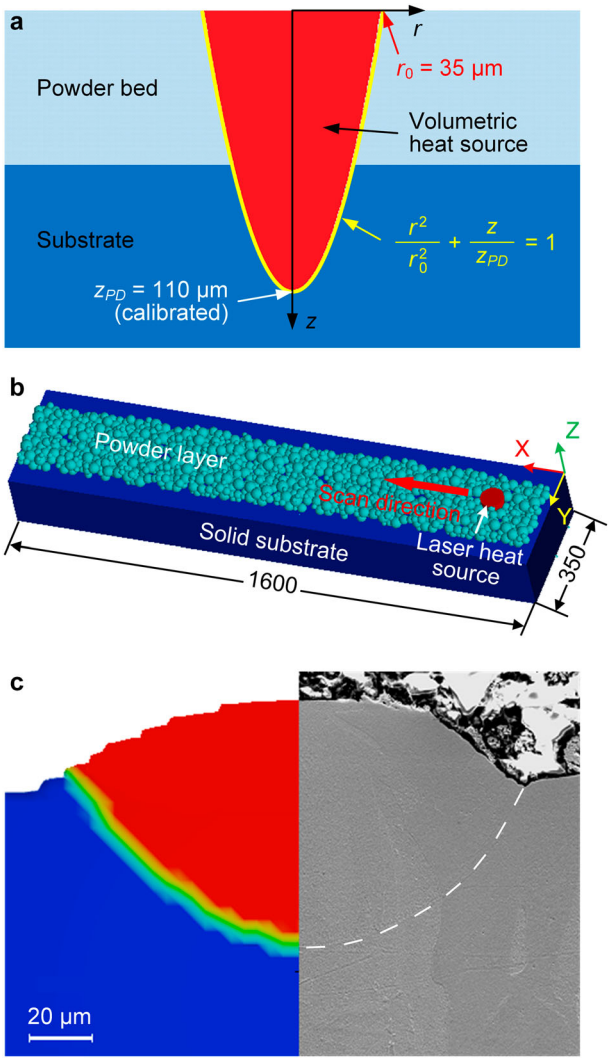

Figure 3. (a) Profile of the volumetric heat source, (b) the model geometry of single-track printing on a solid substrate (unit: μm), and (c) the comparison of melt pool dimensions obtained from the experiment (right half) and simulation (left half) for a calibrated optical penetration depth of 110 μm (laser power 200 W and scan speed 800 mm/s, solidified layer thickness 30 μm, powder size 10–45 μm).

heat source is determined by:

$$r^2/r_0^2 + z/z_{PD} = 1 \quad (5)$$

where r, r_0, z and z_{PD} are the radial coordinate, laser spot radius, depth coordinate, and the optical penetration depth, respectively. The rationale behind the functional form of the volumetric heat source used in Eq. 5 is discussed in Appendix A. The optical penetration depth (i.e. the height of the volumetric heat source) was determined through a series of trial simulations to ensure that model predictions agreed well with the experimentally measured melt pool dimensions. More specifically, simulations of single-track printing on the solid substrate were performed using different optical penetration depths, i.e. setting different heights for the volumetric heat source. The optical penetration depth at which the simulated melt depth was closest to the experimental melt depth was selected as the calibrated optical penetration depth and used in subsequent simulations. In these single-track printing simulations, the process parameters were the same as stated in Section 2.2.2. To simplify the model and ensure easy implementation in the Flow-3D simulation software, the laser power (200 W for the interior solid region) was assumed to be uniformly distributed within the circular paraboloid volume. The model geometry is illustrated in Figure 3b and the comparison of melt pool dimensions obtained from the experiment and simulation is shown in Figure 3c. The calibrated optical penetration depth value of the equivalent volumetric heat source was found to be 110 μm which is physically reasonable since similar melt depths have been measured before in the literature under similar process parameters (Kamath et al. 2014). Figure 3c shows that the calibrated model was capable of predicting the shape and the dimensions of the resulting melt pool accurately.

This calibrated model was used to simulate the L-PBF process of the border tracks in the overhang region. The model geometry is illustrated in Figure 4. The process parameters used in the simulation are listed in Table 2. To save the computational time and cost, the spherical-shaped powder was converted into 32-facet polyhedrons to reduce the number of mesh nodes.

4. Results and discussion

4.1. Melt pool dynamics in the overhang region

The DEM-CFD model described in Section 3 was used to gain physical insight into the formation of surface roughness in overhang regions. The solidified contour of tracks in a 45° overhang region is illustrated in Figure 5. For a 45° overhang region, a solid inner border was printed first followed by an overhang outer border, corresponding to the tracks 1 and 2 in Figure 5, respectively. Tracks 1 and 2 were simulated using the process parameters listed in Table 2. Here, the solidified contour of track 2 was the result of the evolution process shown in Figure 6.

Figure 6 illustrates the evolution of the melt pool in the overhang region (outer border) with a 45° overhang angle. When the laser beam moved towards and then away (perpendicular to the plane) from the area of interest (highlighted in Figure 6 with a dashed rectangle), the powder was first heated by the laser beam and then cooled down due to heat diffusion to surrounding material and the convective Ar atmosphere. Correspondingly, the evolution process of a melt pool can be

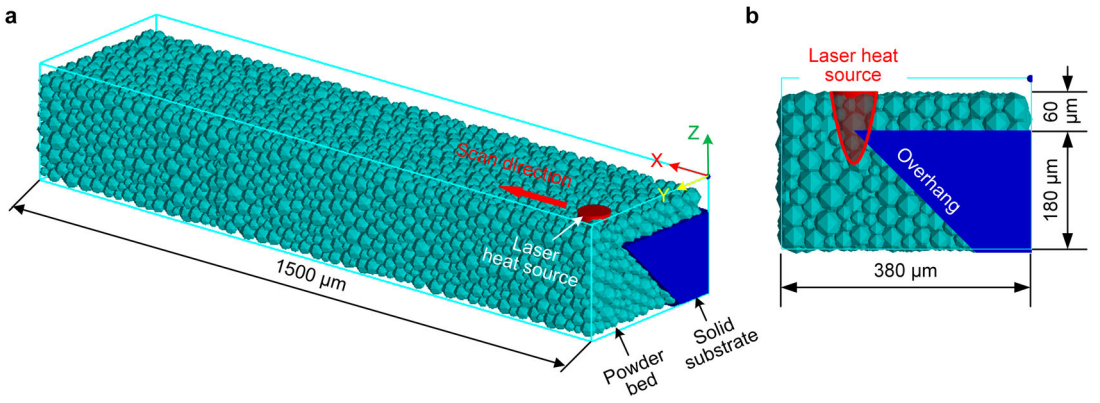

Figure 4. The model geometry of an overhang being L-PBF processed: (a) 3D view and (b) right view.

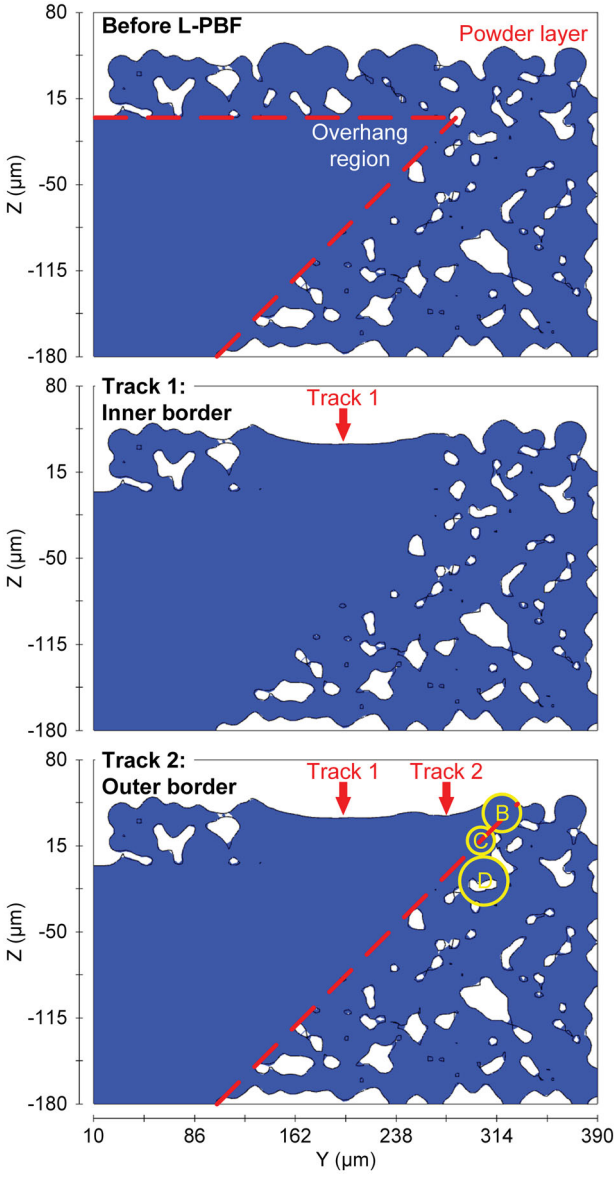

Figure 5. The cross-sectional contour of border tracks in a 45° overhang region.

roughly divided into two stages: melting (including powder melting and gap filling) and solidification. There is a transient duration (875–879 μs) from the melting stage to the solidification stage with no clear demarcation between these two stages. During the melting stage, the powder began to melt forming a melt pool until the melt pool enlarged to the maximum depth and then maximum width. The top of the powder bed (powder particle A in Figure 6) was melted first as it was directly exposed to the laser irradiation. The width and depth of melt pool increased over time as the laser energy was transferred to the surrounding powder mainly via heat conduction. Gaps between powder particles were subsequently filled up by molten metal via the gravity and the capillary effect. Powder at the centre of the melt pool (particle A in Figure 6) was completely melted while powder particles at the border of the melt pool (particles B, C, and D in Figure 6) were partially melted.

In the solid region, the melt pool exists on a dense substrate. The depth of the melt pool in this case is mainly determined by the laser energy transmission and heat transfer inside the substrate but not the gravity or surface tension. On the other hand, both gravity and surface tension have considerable effects on the depth of the melt pool in the overhang region where the melt pool is formed on a powder bed containing many voids. As a result, molten metal flows downwards into the voids inducing the sinking of the melt pool, increasing the depth of melt pool and promoting dross formation. The sinking of the melt pool is thus driven by gravity and surface tension-induced capillary effect. In Figure 6, gaps 2 and 3 were filled via this phenomenon. Melt pool sinking was aided by the temperature-dependent viscosity since high temperatures improved the flowability of the molten metal and thus sunk the melt pool further, and vice versa. At a time of 875 μs, when

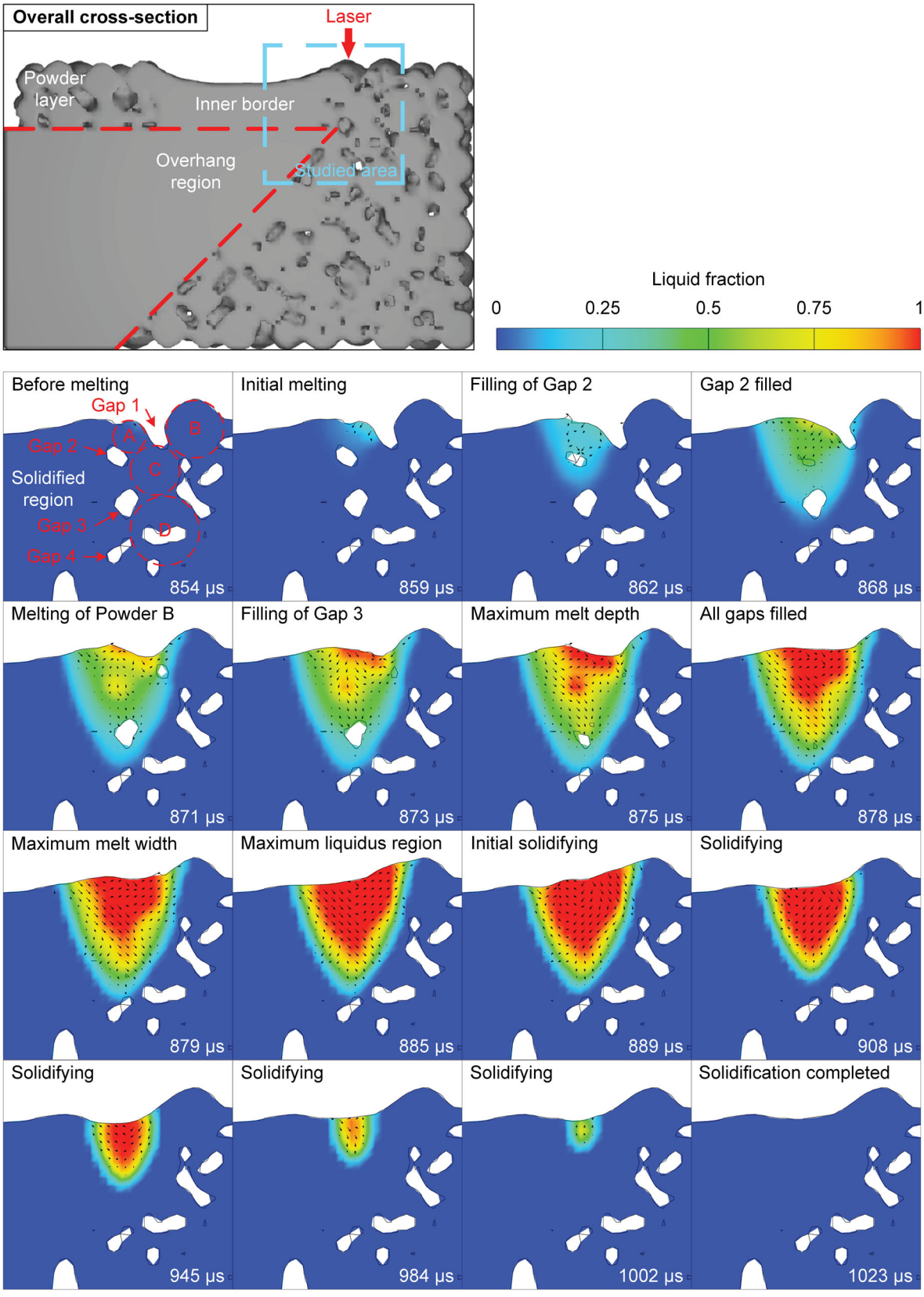

Figure 6. Evolution of melt pool in the overhang region ($\theta = 45°$, $P = 100$ W, $v = 1000$ mm/s, the streamlines are shown by arrows).

the melt pool reached its maximum depth, the upper half of gap 4 was surrounded by the molten metal. However, molten metal was unable to penetrate this gap owing to the limiting effect of viscosity. The molten metal subsequently cooled down and solidified, leaving this gap unfilled as a pore in the overhang region (Figure 10e). It is interesting to note that the melt pool reached its maximum depth (875 μs) and width (879 μs) asynchronously, although the time difference is quite small. Not all the gaps in the melt pool were filled when the melt pool reached its maximum depth. There was a 3 μs lag between maximum melt depth and all gaps being filled. Moreover, the volume of the fully melted region (red region in Figure 6 that the liquid fraction equals 1) reached its maximum at a time of 885 μs, 10 μs later than the maximisation of melt depth and 6 μs later than the maximisation of melt width.

During the solidification stage, the melt pool cooled down and solidified gradually via thermal diffusion into the solidified layers and forced convection of Ar flow. The cooling rate was much lower than the heating rate of the laser due to the extremely high laser power density. Thus, the duration of the solidification stage was around 6 times longer than that of the melting stage. The cross-sectional shape of the solidified melt pool manifested as the track contour.

4.2. The formation mechanism of surface morphology in the overhang region

The surface morphology of an overhang region is mainly determined by a combination of the solidified contour of the border tracks, powder adhesion, and thermal stresses-induced warp deformation, as explained in the subsections below.

4.2.1. Effect of the solidified border contour

Ideally, the overhang region is a flat surface (looking like a straight line in the Y-Z cross-section, as shown in Figure 5), but in reality, border track contours of multilayers manifest themselves as a wavy contour of the overhang region. Powder adhesion due to partial sintering further imparts irregularity to the morphology of this wavy contour, increasing its roughness as discussed in Section 4.2.2. Because the overhang region is an assembly of sliced layers, when not considering powder adhesion, the contour of the overhang region can, in principle, be deduced from the regularly duplicated array of a single-layer contour following the specific overhang angle and layer thickness, as shown in Figure 7. When $\theta \leq 60°$, the contour of inner borders is overwritten by the outer borders (Figure 7a). Therefore, the outer borders are the main contributor to the overhang contour. When $\theta > 60°$, both the inner and outer borders contribute to the overhang contour (Figure 7b). The resulting wavy contour of the overhang region is a source of surface roughness.

4.2.2. Effect of powder adhesion

As discussed in Section 4.1, powder on the edges of the melt pool can be partially melted or sintered, e.g. powder particles B, C, and D in Figures 5 and 6. The remaining unmelted part is exposed to the overhang region (known as powder adhesion), contributing to the surface morphology. When considering powder adhesion, as shown in Figure 8, the contour of the overhang region becomes irregular, thus enhancing the surface roughness. Although powder adhesion is stochastic in nature, both the experimental and simulation results indicated that there are statistical correlations between the process parameters (overhang angle, laser power, and scan speed) and the surface roughness of the overhang region. Powder adhesion is the main contributor to surface roughness in the overhang region. In addition to powder adhesion, the solidified border contour and warp deformation jointly enhance surface roughness when $\theta > 45°$. Further discussion will be presented in Section 4.3.1.

4.2.3. Effect of warp deformation of the overhang region

When printing an overhang region without supports, thermal stresses induce warp deformation in the overhang region due to the lack of constraints. Although warp deformation is a measure of macro shape deviations, it has a combined effect with the other two influencing factors (border track contour and powder adhesion) on the surface roughness of the overhang region. As discussed in Section 4.2.1, the contour of the border tracks determines the morphology of an overhang region. The contour of the overhang region is determined by the relative position relationship between the border tracks of adjacent layers. When $\theta \leq 45°$, the effect of warp deformation is negligible, as shown in Figure 9a, b and c. The offset of the border contour of layer $i+1$ with respect to the border contours of layer i is calculated by

$$\Delta_V = t \tag{6}$$

$$\Delta_H = t \cdot \tan\theta \tag{7}$$

where Δ_V, Δ_H, and t are vertical offset, horizontal offset, and layer thickness, respectively.

When $\theta > 45°$, the effect of warp deformation on the contour offset has to be taken into account, as shown in Figure 9d and e. The warp deformation mainly

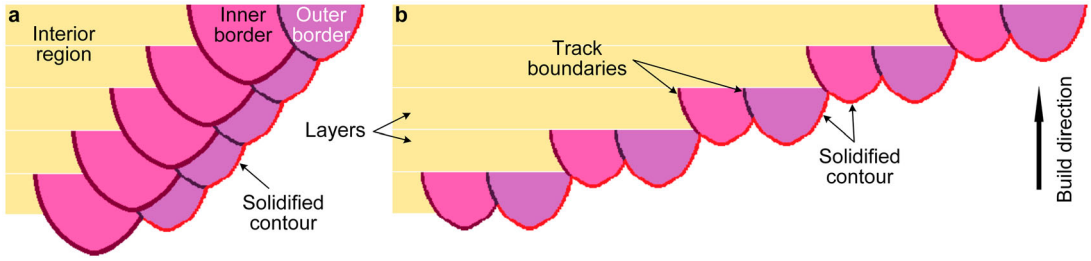

Figure 7. The overhang contour is contributed by (a) only outer borders when $\theta \leq 60°$ (b) both inner borders and outer borders when $\theta > 60°$.

induces shape deviations in the vertical direction while its effect in the horizontal direction is negligible. The vertical offset of layer $i+1$ with respect to layer i was estimated by Kamat *et al*. (Kamat and Pei 2019) to be:

$$\Delta_V = t + \frac{6\sigma_y m t \tan^2\theta}{E}\left\{\sum_{j=i+1}^{n}\left[\ln\left(\frac{j-i+1}{j-i}\right)-\frac{1}{j+1}\right] -\ln(i+1)+\frac{i}{i+1}\right\} \quad (8)$$

where σ_y, m, n, j, and E are yield stress, melt depth-to-layer thickness ratio, number of total layers, index of summation ($i+1 \leq j \leq n$), and Young's modulus, respectively. It is concluded from Eq. 8 that the warp deformation-induced contour offset becomes more considerable with the increase of the overhang angle.

4.3. Effect of overhang angle on surface roughness in the overhang region

4.3.1. Estimation of the surface roughness in the overhang region from simulation

As discussed in Section 4.2, the surface roughness in the overhang region is a result of the combined effect of border track contour, powder adhesion and warp deformation. In light of this conclusion, the 2D multi-layer contour of the L-PBF printed overhang region can be approximated using the simulation results of border tracks by taking into account the powder adhesion and warp deformation-induced contour offset (Eqs. 6–8). Specifically, seven cross-sections were selected randomly from the overhang region and then arrayed according to the calculated offsets in horizontal and vertical directions (as shown in Figure 10a and b). Profiles of the border tracks including the adhered powder particles were extracted as the predicted multi-layer overhang contour, as shown in Figure 11. This approximation is a more efficient and economical way to simulate the micro surface deviation of overhang regions and estimate the surface roughness as 3D multi-layer simulations are much more complicated and cost-intensive.

The simulation-predicted 2D contours of the overhang regions with various overhang angles are extracted and plotted in Figure 11. The dashed lines indicate the planar profile of designed overhang region specified by the overhang angles. R_a was calculated by averaging the contour offset from the reference line:

$$R_a = \frac{1}{L}\int_0^L |\delta(x)|dx \quad (9)$$

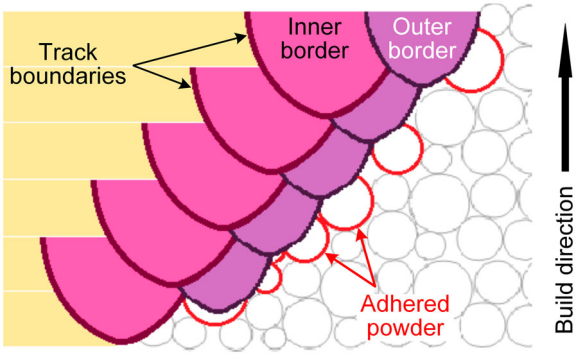

Figure 8. Schematic of powder adhesion on a 45° overhang region.

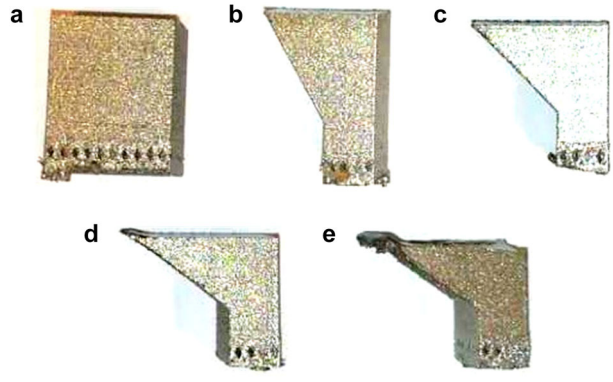

Figure 9. The L-PBF printed samples with various overhang angle (a) $\theta = 0°$ (cube), (b) $\theta = 30°$, (c) $\theta = 45°$, (d) $\theta = 55°$ and (e) $\theta = 60°$.

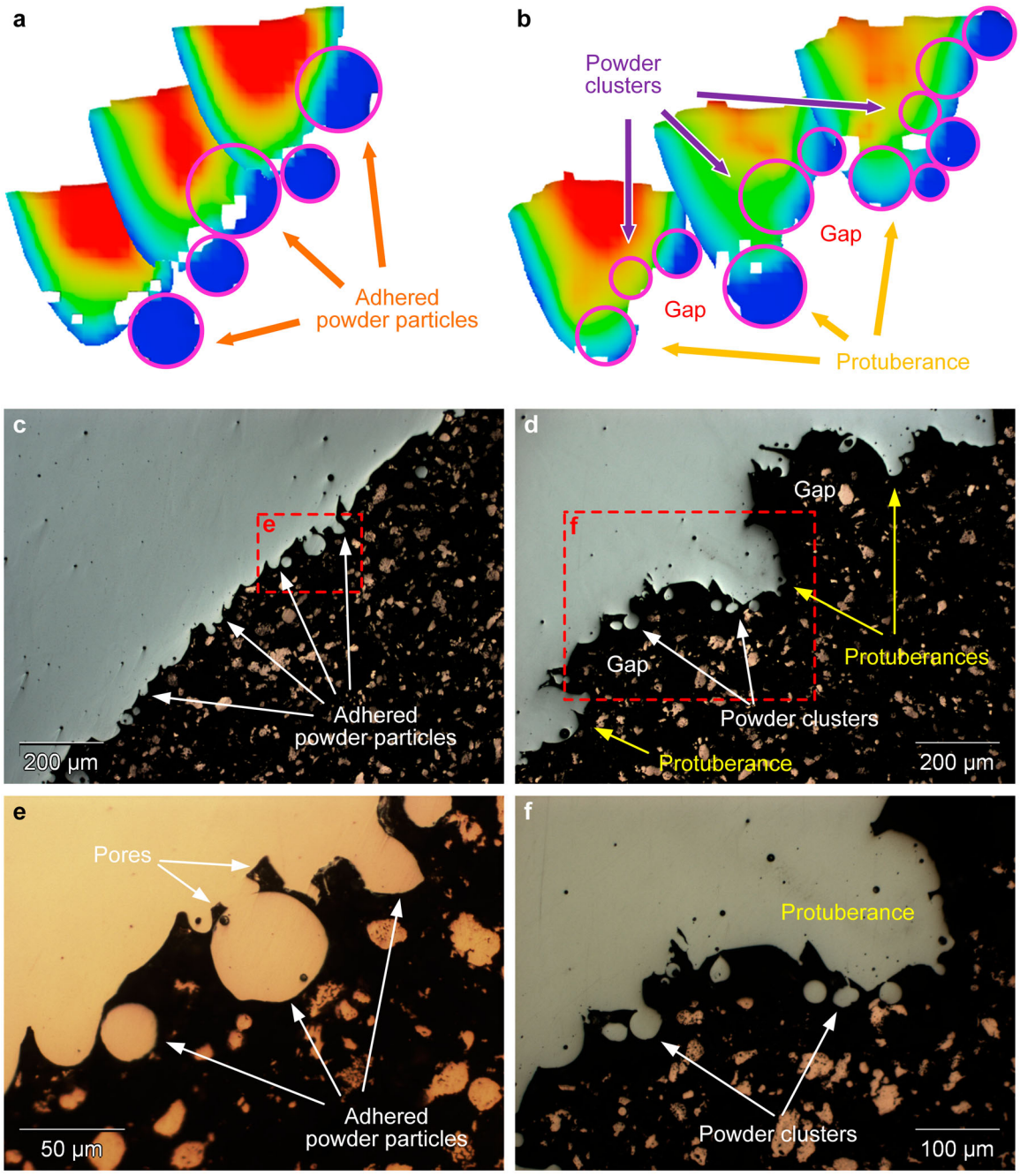

Figure 10. Two mechanisms of powder adhesion related to the overhang angle: (a) simulation-predicted, $\theta = 45°$; (b) simulation-predicted, $\theta = 60°$; (c, e) optical micrographs, $\theta = 45°$; (d, f) optical micrographs, $\theta = 60°$. (e) and (f) are partial enlargement of (c) and (d), respectively.

where x is the coordinate parallel to the reference line, δ is the contour offset from the reference line and is a function of x, and L is the sampling length (varying from 210 μm to 1209 μm depending upon the overhang angle). It is seen that the powder particles adhered to the overhang region forming surface roughness. The contour was in good accordance with the reference line when $\theta \leq 45°$, while a deviation between the contour and the reference line became noticeable when $\theta > 45°$. This deviation was due to the warp deformation discussed in Section 4.2.3. For a sampling length of 1190 μm when $\theta = 80°$, according to Eq. 8, the deviation in the vertical direction was as large as 123 μm. Thus, the contour deviated largely from the reference line at $\theta = 80°$, as shown in Figure 11e.

The experimentally measured R_a in overhang regions is shown in Figure 12a as a function of varying overhang angle. Overall, R_a increased with increasing overhang angle. Moreover, it was found that the effect of measuring direction was less significant, indicating that R_a was isotropic and independent of direction.

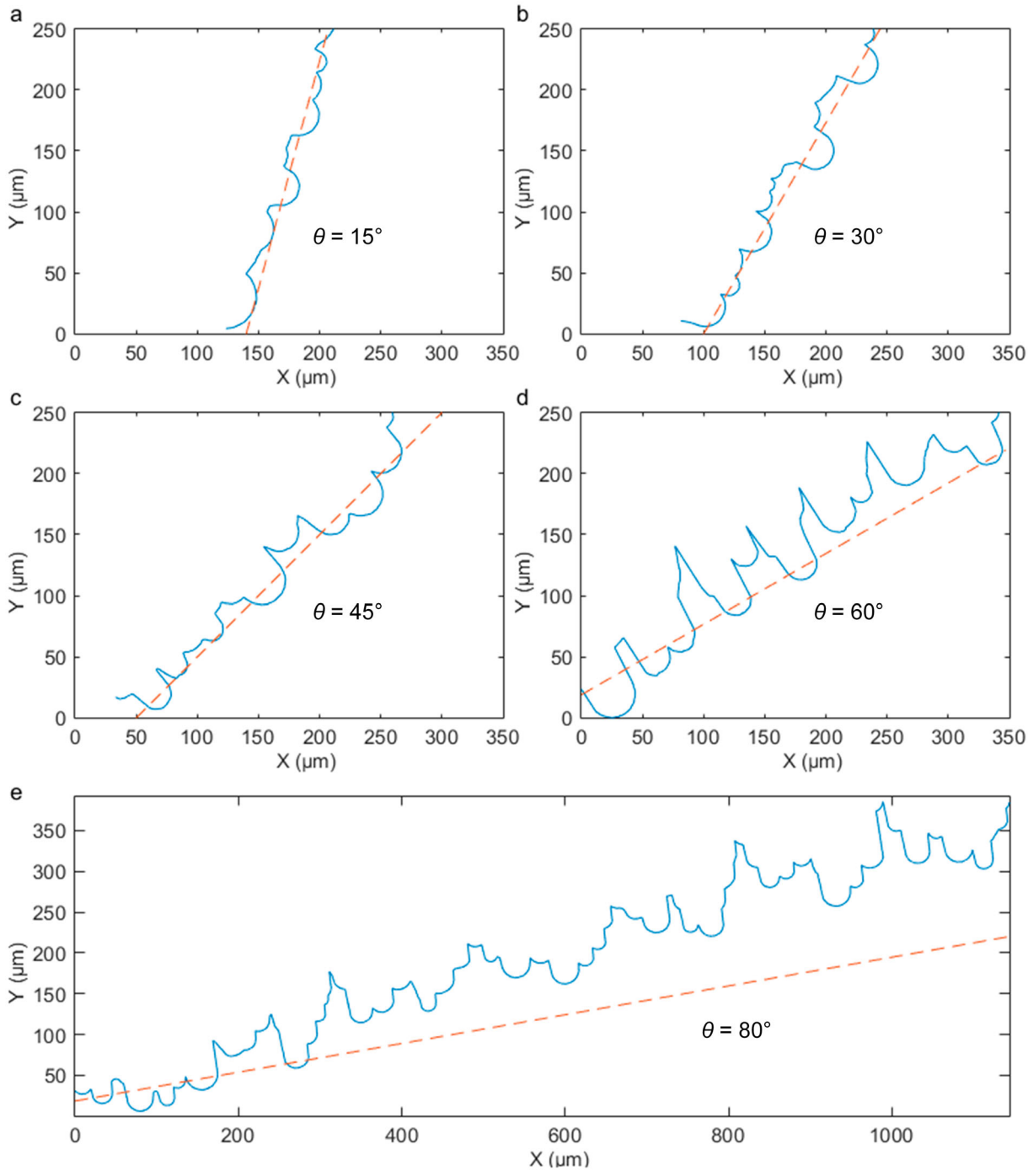

Figure 11. Simulation-predicted surface morphology in the overhang region at different overhang angle: (a) $\theta = 15°$, (b) $\theta = 30°$, (c) $\theta = 45°$, (d) $\theta = 60°$ and (e) $\theta = 80°$ (Blue solid lines: simulation-predicted contour; red dashed lines: the planar profile of designed overhang region specified by the overhang angles).

A comparison of simulation-predicted R_a and experimentally measured R_a is shown in Figure 12b. Here, both the experimental and simulation-predicted roughness values were normalised to the reference value of R_a at 0° overhang angle. It should be noted that the absolute value of the simulation-predicted R_a is smaller than the experimental results (around half of the experimental result when $\theta = 0°$) because the sampling length in the simulation is much smaller than the specified value in ISO 4288, making some deviation information unavailable. In general, the simulation-predicted trend of R_a was consistent with the experimental results although there was a discrepancy when $\theta \geq 60°$ due to the considerable but unpredictable dross in the overhang region.

The overhang angle is the most important structural parameter for an overhang region, indicating the

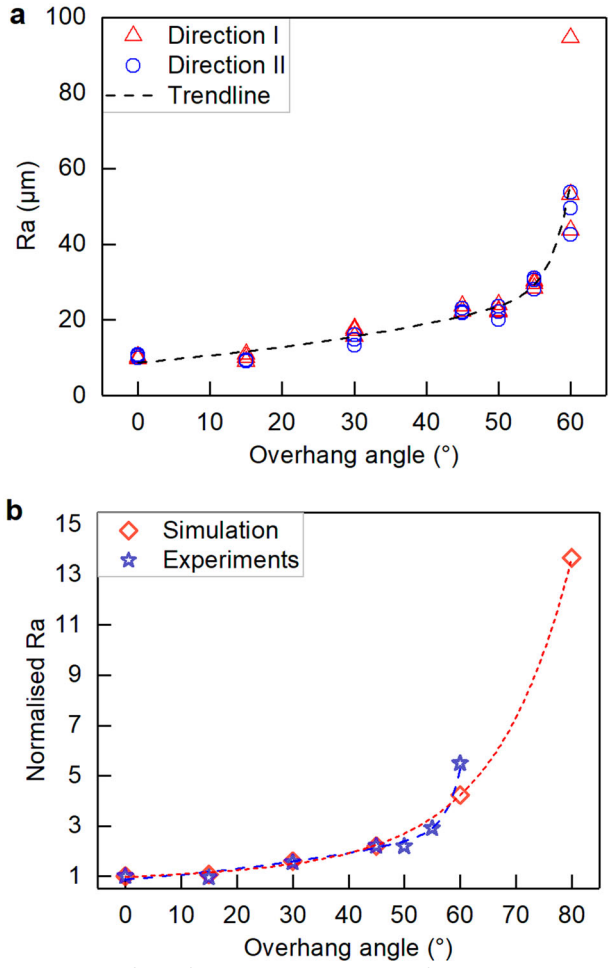

Figure 12. Effect of overhang angle on surface roughness R_a in overhang regions: (a) experimental results; (b) a comparison of simulation-predicted R_a and experimental R_a, both normalised to the reference value of R_a at $\theta = 0°$.

degree of inclination of an overhang region and determining the difficulty of L-PBF. The overhang angle plays a decisive role in the surface morphology and shape deviations on both the macroscale and microscale, influencing stress-induced deformation and surface roughness, respectively. On the macroscale, as shown in Figures 9 and 11, the L-PBF printed samples displayed good shape accuracy when $\theta \leq 45°$, while shape deviations became a considerable problem visible to the naked eye when $\theta > 45°$. The shape deviation was mainly caused by the upward warp at the overhang tip. This was especially significant when the overhang angle was as large as 60° where severe warpage and dross were observed at the tip. On the microscale, meanwhile, surface morphology became rougher gradually with increasing overhang angle, indicating an increase of surface roughness on the overhang region, as shown in Figures 11 and 12a.

From the simulation and experimental results, the changing trend of R_a with the overhang angle can be roughly divided into three regimes (Figures 11 and 12a). First, there was no change of R_a with the increasing overhang angle until $\theta = 15°$. Then, R_a gradually increased with the increase of overhang angle when $15° < \theta < 50°$. The rate of change of R_a with respect to overhang angle increased sharply at $\theta = 50°$, after which the R_a curve increased rapidly. The relation between the surface roughness of the overhang region and the overhang angle was mainly established by the mechanisms of powder adhesion, where powder or powder clusters protruded from the surface (Figure 13).

The mechanisms of powder adhesion were strongly related to the overhang angle. In other words, different ranges of overhang angle displayed different mechanisms of powder adhesion. R_a at $\theta = 0°$ was considered the benchmark for comparison. Here, there was no overhang region, and the melt pool was fully supported by the previously printed layer (substrate). Only a small area of the melt pool boundaries directly contacted the powder bed at the side which resulted in slight powder adhesion on the side walls. When $\theta \leq 15°$, the overhang angle was small enough and thus its effect on R_a was negligible (Figures 11a and 13a).

When the overhang angle ranged from 15° to 50°, part of the melt pool was supported by the powder bed. This implied: (a) the weakness of the support of the melt pool, promoting the sinking of the melt pool and inducing more molten metal flowed downwards into the gaps between powder particles; (b) the increase of contact area between the melt pool boundary and powder bed. Both of these two factors resulted in more powder particles being adhered, promoting powder adhesion and thus increasing R_a (Figures 11b, 11c, 13b and 13c).

When the overhang angle increased further ($\theta > 50°$), in addition to the influencing factors discussed above (melt pool sinking and increase of the contact area between the melt pool boundary and powder bed), several other unfavourable factors contributed jointly to the mechanism of powder adhesion, such as border track-induced waviness of the overhang contour, warp deformation, and dross formation. As discussed in Section 4.2.1, the solidified contour of the melt pool of border tracks manifested as the wavy contour of the overhang region (without taking into account the adhered powder particles). It is seen in Figure 10a and c that the waviness at $\theta = 45°$ was not very large, indicating that the border track contour was not a significant influencing factor on surface roughness. In contrast, the waviness of the 60° overhang region (Figure 10b and d) was much larger than that of the 45° overhang region, making the border track contour a considerable influencing factor. The wavy contour consisted of a

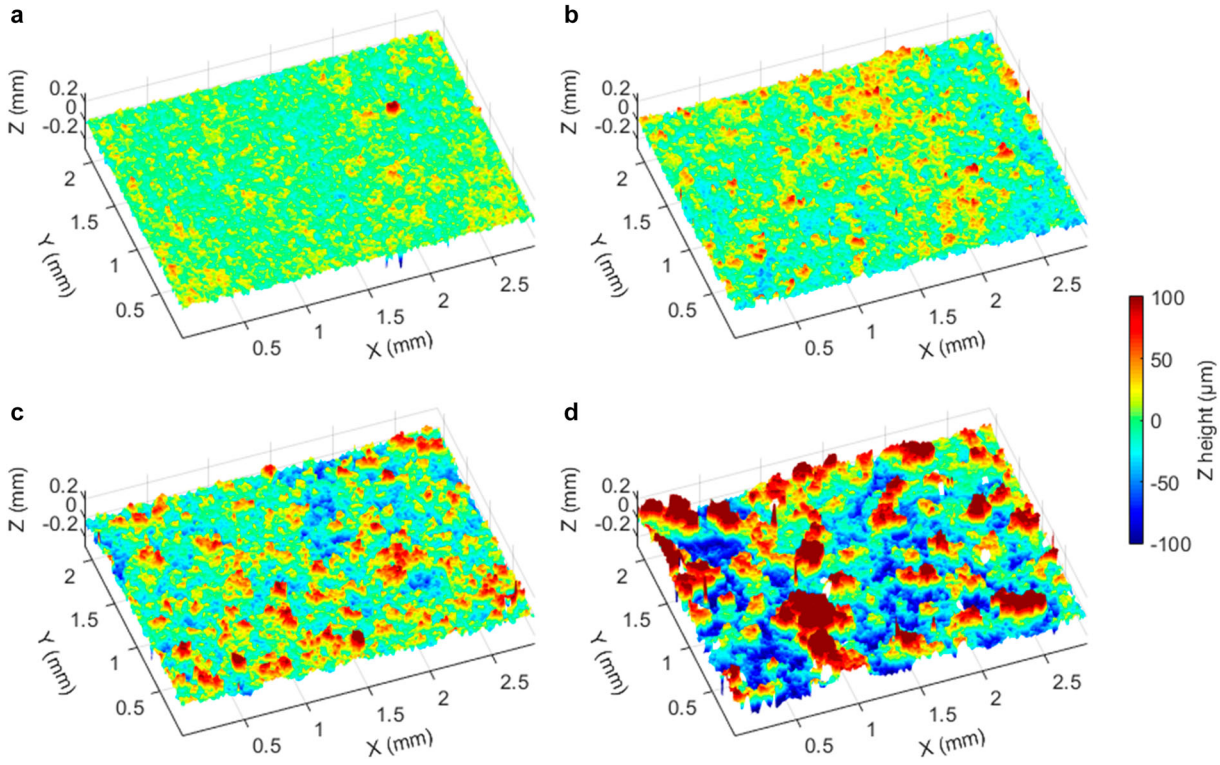

Figure 13. Surface morphology of L-PBF printed overhang regions with different overhang angle: (a) $\theta = 15°$, (b) $\theta = 30°$, (c) $\theta = 45°$ and (d) $\theta = 60°$ (overhang border parameters: $P = 100$ W, $v = 1000$ mm/s).

number of undesired protuberances due to over-melting into the loose powder bed. Powder particles adhered to the protuberances forming powder clusters; meanwhile, gaps were manifested between the powder clusters (Figures 10b, d, f and 13d). This was a significant contributor to surface roughness when $\theta \geq 60°$. Moreover, severe warp deformation and dross also played noticeable roles in contributing to the surface roughness of the overhang region, as shown in Figure 11d and e. Warp deformation and dross were the most crucial factors influencing the surface roughness of the overhang region when the overhang angle increased up to 80°, while the exposure of the inner border contour further enhanced the contour waviness and surface roughness (Figure 11e). The three regimes of powder adhesion related to the overhang angle are summarised in Table 4.

It can be concluded from the preceding discussion that the critical overhang angle is a threshold not only for macro deformations but also for micro shape deviations, which, in the present study, is around 50°. It should be noted that the overhang region with a constant overhang angle of 80° cannot be printed successfully because this large overhang angle results in the collapse of the overhang region during the printing process. But the simulation study on 80° overhang region will benefit the printing of overhang regions with a continuously changing overhang angle (such as horizontal circular channels) which is a challenging task in L-PBF.

The experimental results (Figure 12a) showed that when $\theta \leq 55°$, the distance from the start point had an insignificant effect on the overhang R_a. In other words,

Table 4. Three regimes of powder adhesion related to the overhang angle.

Overhang angle	Regime of powder adhesion
$0° \leq \theta \leq 15°$	(i) A small area of the melt pool boundaries contacts the powder bed resulting in slight powder adhesion on the side walls (ii) The effect of overhang angle is not significant
$15° < \theta \leq 50°$	Powder adhesion is enhanced by: (i) the sinking of the melt pool (ii) the increase of contact area between the melt pool boundary and powder bed
$\theta > 50°$	Powder adhesion is further promoted and Ra increases sharply due to the combination of: (i) the enhanced sinking of the melt pool (ii) the further increase of contact area between the melt pool boundary and powder bed (iii) large waviness of the overhang contour and the induced powder clusters (iv) severe warp deformation and dross

the surface roughness was generally homogeneous on the overhang regions when $\theta \leq 55°$. On the other hand, however, the experimental results showed a strong trend that R_a increased with increasing the distance from the start point of the overhang when $\theta = 60°$. This also indicated that severe warp deformation and dross had a combined effect on R_a since those unfavourable factors became more considerable with increasing the length of the overhang region when $\theta = 60°$.

4.3.2. Potential solutions to mitigate surface roughness issue in the overhang region

The volumetric energy density determined the volume and the fluidity of the molten metal. Higher laser energy induced a higher temperature in the melt pool. Firstly, this led to more metal melting, forming a larger melt pool and enlarging the contact area of the melt pool boundaries with the powder bed. Secondly, this resulted in better flowability of the molten metal, causing more molten metal to flow downwards into the gaps between powder particles and promoting the sinking of the melt pool. As discussed in Section 4.3.1, both of these two factors resulted in more powder particles being partially melted or sintered, enhancing powder adhesion and thus increasing R_a. Besides, increasing volumetric energy density can also lead to overheating of the powder bed, exacerbating dross formation on the overhang region and further increasing R_a.

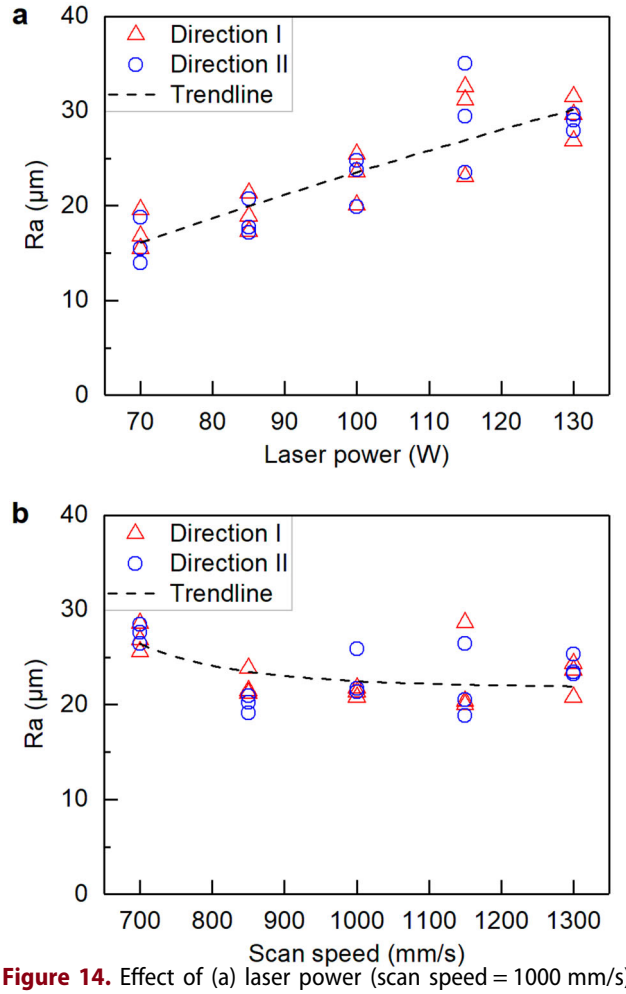

Figure 14. Effect of (a) laser power (scan speed = 1000 mm/s) and (b) scan speed (lase power = 100 W) on surface roughness R_a in overhang regions ($\theta = 45°$, laser power and scan speed referred to overhang border parameters, and the other process parameters are listed in Table 2).

Therefore, a potential solution to mitigate the high surface roughness issue in L-PBF printed overhang regions is to adjust the process parameters to decrease volumetric energy density (such as decreasing laser power or increasing scan speed) when printing overhang regions. From the experimental results shown in Figure 14a, decreasing laser power was an effective way to decrease R_a, which confirmed the previous conjecture. On the other hand, however, R_a did not decrease significantly with increasing scan speed (Figure 14b) although this decreased the volumetric energy density. The reason may be that increasing scan speed enhanced the discontinuity of the overhang track, inducing a rougher overhang surface (Le et al. 2020). About the optimisation and feed-forward control of laser power to decrease R_a of overhang regions, more studies need to be conducted in the future.

5. Conclusions

This study investigated the evolution and formation mechanisms of surface morphology in the laser powder bed fused overhang region, taking into account the effects of overhang angle, laser power, and scan speed on surface roughness R_a of the overhang region using single-factor experiments and a coupled DEM-CFD simulation model. The main conclusions are summarised as follows.

(1) The melt pool in the overhang region is weakly supported by the powder bed. Molten metal flows downwards into the voids driven by gravity and surface tension-induced capillary effect, inducing sinking of the melt pool. Melt pool sinking is a contributor to powder adhesion as it increases the melt depth compared to the solid region and makes more powder particles being adhered. Melt pool sinking is governed by the overhang angle and volumetric energy density (related to the temperature field of the melt pool). An increasing overhang angle (weakening the support to the melt pool) or an increasing volumetric energy density (improving the fluidity of

the molten metal) can enhance melt pool sinking and vice versa.

(2) The evolution of surface morphology is the result of a combination of border track contour, powder adhesion, and shape deviations (warp deformation and dross). The contribution of these influencing factors to surface roughness depends on the overhang angle. Powder adhesion is the main influencing factor to surface roughness, and border contour and shape deviations enhance surface roughness further when $\theta > 45°$. The contours of border tracks manifest as the wavy basal contour of an overhang region. For overhang angle $\theta \leq 60°$, only outer border tracks contribute to the overhang contour. When $\theta > 60°$, both outer and inner border tracks affect the overhang contour.

(3) The effect of the overhang angle on surface roughness of an overhang region can be divided into three regimes according to the mechanisms of powder adhesion and formation of micro shape deviations. When $0° \leq \theta \leq 15°$, the overhang angle has no significant influence on R_a. When $15° < \theta \leq 50°$, R_a increases because of powder adhesion being promoted by (a) increasing contact area between the melt pool boundaries and powder bed, and (b) sinking of the melt pool. When $\theta > 50°$, R_a increases sharply under the combined effect of powder adhesion, large wavy contour and the induced powder clusters, and severe warp deformation and dross. When the overhang angle increases up to 80°, warp deformation and dross play the most crucial role in determining R_a.

(4) R_a increases with increasing laser power since the increase of volumetric energy density enlarges the contact area of the melt pool boundaries with the powder bed and promotes melt pool sinking, thus enhancing powder adhesion in the process.

Acknowledgements

The authors thank Dr. Redmer van Tijum (Philips Personal Care, Drachten, the Netherlands) for his help with the surface morphology/roughness measurements.

Disclosure statement

No potential conflict of interest was reported by the author(s).

Funding

This work was financially supported by Beijing Natural Science Foundation (3214049); Fundamental Research Funds for the Central Universities, China (FRF-TP-18-055A1); the Partnership Program (project number 15808/S16044) of the Materials innovation institute M2i (www.m2i.nl) and the Technology Foundation TTW (www.stw.nl), which is part of the Netherlands Organization for Scientific Research (www.nwo.nl); and the ICD Advanced Additive program (Innovation Cluster Drachten, the Netherlands). Amar M. Kamat acknowledges financial support from the ITEA Daytime project (ITEA-2018-17030-Daytime).

Notes on contributors

Shaochuan Feng is currently a postdoctoral researcher at the University of Groningen in the Netherlands and University of Science and Technology Beijing in China. His research interest focuses on additive manufacturing of metals, laser materials processing and technology, and analytical and computational modelling.

Amar M. Kamat is currently a postdoctoral researcher at the University of Groningen in the Netherlands. His research interests lie in additive manufacturing, laser materials processing, bioinspired sensors, and flexible electronics.

Soheil Sabooni is currently a postdoctoral researcher at the University of Groningen in the Netherlands. His research is mainly focusing on materials science, additive manufacturing, and surface engineering.

Yutao Pei is currently a professor at the University of Groningen in the Netherlands. His main research interests include additive manufacturing of metals, laser materials processing and technology, nanostructured materials for energy storage, and surface and interface science.

ORCID

Shaochuan Feng http://orcid.org/0000-0003-3406-0290
Amar M. Kamat http://orcid.org/0000-0002-1622-9067
Yutao Pei http://orcid.org/0000-0002-1817-2228

References

Cai, Chao, Chrupcala Radoslaw, Jinliang Zhang, Qian Yan, Shifeng Wen, Bo Song, and Yusheng Shi. 2019. "In-Situ Preparation and Formation of TiB/Ti-6Al-4V Nanocomposite via Laser Additive Manufacturing: Microstructure Evolution and Tribological Behavior." *Powder Technology* 342: 73–84. doi:10.1016/j.powtec.2018.09.088.

Cai, Chao, Wei Shian Tey, Jiayao Chen, Wei Zhu, Xingjian Liu, Tong Liu, Lihua Zhao, and Kun Zhou. 2021. "Comparative Study on 3D Printing of Polyamide 12 by Selective Laser Sintering and Multi Jet Fusion." *Journal of Materials Processing Technology* 288 (August 2020): 116882. doi:10.1016/j.jmatprotec.2020.116882.

Cai, Chao, Xu Wu, Wan Liu, Wei Zhu, Hui Chen, Jasper Dong Qiu Chua, Chen Nan Sun, Jie Liu, Qingsong Wei, and Yusheng Shi. 2020. "Selective Laser Melting of Near-α Titanium Alloy Ti-6Al-2Zr-1Mo-1V: Parameter Optimization, Heat Treatment and Mechanical Performance." *Journal of*

Materials Science and Technology 57: 51–64. doi:10.1016/j.jmst.2020.05.004.

Charles, Amal, Ahmed Elkaseer, Lore Thijs, and Steffen G. Scholz. 2020. "Dimensional Errors Due to Overhanging Features in Laser Powder Bed Fusion Parts Made of Ti-6Al-4V." *Applied Sciences* 10 (7): 2416. doi:10.3390/app10072416.

Chatham, Camden A., Timothy E. Long, and Christopher B. Williams. 2019. "A Review of the Process Physics and Material Screening Methods for Polymer Powder Bed Fusion Additive Manufacturing." *Progress in Polymer Science* 93: 68–95. doi:10.1016/j.progpolymsci.2019.03.003.

Du, Yang, Xinyu You, Fengbin Qiao, Lijie Guo, and Zhengwu Liu. 2019. "A Model for Predicting the Temperature Field during Selective Laser Melting." *Results in Physics* 12 (November 2018): 52–60. doi:10.1016/j.rinp.2018.11.031.

Duval-Chaneac, M. S., S. Han, C. Claudin, F. Salvatore, J. Bajolet, and J. Rech. 2018. "Experimental Study on Finishing of Internal Laser Melting (SLM) Surface with Abrasive Flow Machining (AFM)." *Precision Engineering* 54 (July 2017): 1–6. doi:10.1016/j.precisioneng.2018.03.006.

Feng, Shaochuan, Shijie Chen, Amar M. Kamat, Ru Zhang, Mingji Huang, and Liangcai Hu. 2020. "Investigation on Shape Deviation of Horizontal Interior Circular Channels Fabricated by Laser Powder Bed Fusion." *Additive Manufacturing* 36 (December): 101585. doi:10.1016/j.addma.2020.101585.

Feng, Shaochuan, Chuanzhen Huang, Jun Wang, Hongtao Zhu, Peng Yao, and Zhanqiang Liu. 2017. "An Analytical Model for the Prediction of Temperature Distribution and Evolution in Hybrid Laser-Waterjet Micro-Machining." *Precision Engineering* 47: 33–45. doi:10.1016/j.precisioneng.2016.07.002.

Feng, Shaochuan, Amar M. Kamat, and Yutao Pei. 2021. "Design and Fabrication of Conformal Cooling Channels in Molds: Review and Progress Updates." *International Journal of Heat and Mass Transfer*. doi:10.1016/j.ijheatmasstransfer.2021.121082.

Flow-3D V11.2 Documentation. 2016. Flow Science, Inc.

Foroozmehr, Ali, Mohsen Badrossamay, Ehsan Foroozmehr, and Sa'id Golabi. 2016. "Finite Element Simulation of Selective Laser Melting Process Considering Optical Penetration Depth of Laser in Powder Bed." *Materials and Design* 89: 255–263. doi:10.1016/j.matdes.2015.10.002.

"Geometrical Product Specifications (GPS) — Surface Texture: Profile Method — Rules and Procedures for the Assessment of Surface Texture (ISO 4288)." 1996. International Organization for Standardization. https://www.iso.org/standard/2096.html.

Günther, Johannes, Stefan Leuders, Peter Koppa, Thomas Tröster, Sebastian Henkel, Horst Biermann, and Thomas Niendorf. 2018. "On the Effect of Internal Channels and Surface Roughness on the High-Cycle Fatigue Performance of Ti-6Al-4V Processed by SLM." *Materials & Design* 143: 1–11. doi:10.1016/j.matdes.2018.01.042.

Hopkinson, Neil, and Phill Dickens. 2000. "Conformal Cooling and Heating Channels Using Laser Sintered Tools." In *Solid Freeform Fabrication Conference*, 490–497. Texas. doi:10.26153/tsw/3075.

Hu, Zhiheng, Haihong Zhu, Changchun Zhang, Hu Zhang, Ting Qi, and Xiaoyan Zeng. 2018. "Contact Angle Evolution during Selective Laser Melting." *Materials and Design* 139: 304–313. doi:10.1016/j.matdes.2017.11.002.

Hu, Cheng, Kejia Zhuang, Jian Weng, and Donglin Pu. 2019. "Three-Dimensional Analytical Modeling of Cutting Temperature for Round Insert Considering Semi-Infinite Boundary and Non-Uniform Heat Partition." *International Journal of Mechanical Sciences* 155 (October 2018): 536–553. doi:10.1016/j.ijmecsci.2019.03.019.

Huang, Yuze, Mir Behrad Khamesee, and Ehsan Toyserkani. 2019. "A New Physics-Based Model for Laser Directed Energy Deposition (Powder-Fed Additive Manufacturing): From Single-Track to Multi-Track and Multi-Layer." *Optics & Laser Technology* 109 (August 2018): 584–599. doi:10.1016/j.optlastec.2018.08.015.

Kadirgama, K., W. S. W. Harun, F. Tarlochan, M. Samykano, D. Ramasamy, Mohd Zaidi Azir, and H. Mehboob. 2018. "Statistical and Optimize of Lattice Structures with Selective Laser Melting (SLM) of Ti6AL4V Material." *International Journal of Advanced Manufacturing Technology* 97 (1–4): 495–510. doi:10.1007/s00170-018-1913-1.

Kamat, Amar M, and Yutao Pei. 2019. "An Analytical Method to Predict and Compensate for Residual Stress-Induced Deformation in Overhanging Regions of Internal Channels Fabricated Using Powder Bed Fusion." *Additive Manufacturing* 29 (March): 100796. doi:10.1016/j.addma.2019.100796.

Kamath, Chandrika, Bassem El-Dasher, Gilbert F. Gallegos, Wayne E. King, and Aaron Sisto. 2014. "Density of Additively-Manufactured, 316L SS Parts Using Laser Powder-Bed Fusion at Powers up to 400 W." *International Journal of Advanced Manufacturing Technology* 74 (1–4): 65–78. doi:10.1007/s00170-014-5954-9.

Karimi, J., C. Suryanarayana, I. Okulov, and K. G. Prashanth. 2020. "Selective Laser Melting of Ti6Al4V: Effect of Laser Re-Melting." *Materials Science and Engineering A* (July): 140558. doi:10.1016/j.msea.2020.140558.

Khairallah, Saad A., and Andy Anderson. 2014. "Mesoscopic Simulation Model of Selective Laser Melting of Stainless Steel Powder." *Journal of Materials Processing Technology* 214 (11): 2627–2636. doi:10.1016/j.jmatprotec.2014.06.001.

Khairallah, Saad A., Andrew T. Anderson, Alexander Rubenchik, and Wayne E. King. 2016. "Laser Powder-Bed Fusion Additive Manufacturing: Physics of Complex Melt Flow and Formation Mechanisms of Pores, Spatter, and Denudation Zones." Edited by Adedeji B. Badiru, Vhance V. Valencia, and David Liu. *Acta Materialia* 108 (April): 36–45. doi:10.1016/j.actamat.2016.02.014.

Kuo, C. N., C. K. Chua, P. C. Peng, Y. W. Chen, S. L. Sing, S. Huang, and Y. L. Su. 2020. "Microstructure Evolution and Mechanical Property Response via 3D Printing Parameter Development of Al–Sc Alloy." *Virtual and Physical Prototyping* 15 (1): 120–129. doi:10.1080/17452759.2019.1698967.

Le, K. Q., C. H. Wong, K. H. G. Chua, C. Tang, and H. Du. 2020. "Discontinuity of Overhanging Melt Track in Selective Laser Melting Process." *International Journal of Heat and Mass Transfer* 162 (December): 120284. doi:10.1016/j.ijheatmasstransfer.2020.120284.

Lee, Y. S., and W. Zhang. 2016. "Modeling of Heat Transfer, Fluid Flow and Solidification Microstructure of Nickel-Base Superalloy Fabricated by Laser Powder Bed Fusion." *Additive Manufacturing* 12: 178–188. doi:10.1016/j.addma.2016.05.003.

Leitz, K. H., P. Singer, A. Plankensteiner, B. Tabernig, H. Kestler, and L. S. Sigl. 2017. "Multi-Physical Simulation of Selective

Laser Melting." *Metal Powder Report* 72 (5): 331–338. doi:10.1016/j.mprp.2016.04.004.

Li, Jian, Jing Hu, Yi Zhu, Xiaowen Yu, Mengfei Yu, and Huayong Yang. 2020. "Surface Roughness Control of Root Analogue Dental Implants Fabricated Using Selective Laser Melting." *Additive Manufacturing* 34 (September 2019): 101283. doi:10.1016/j.addma.2020.101283.

Li, Yingli, Kun Zhou, Pengfei Tan, Shu Beng Tor, Chee Kai Chua, and Kah Fai Leong. 2018. "Modeling Temperature and Residual Stress Fields in Selective Laser Melting." *International Journal of Mechanical Sciences* 136 (February): 24–35. doi:10.1016/j.ijmecsci.2017.12.001.

Mazur, Maclej, Martin Leary, Matthew McMillan, Joe Elambasseril, and Milan Brandt. 2016. "SLM Additive Manufacture of H13 Tool Steel with Conformal Cooling and Structural Lattices." *Rapid Prototyping Journal* 22 (3): 504–518. doi:10.1108/RPJ-06-2014-0075.

Mingear, Jacob, Bing Zhang, Darren Hartl, and Alaa Elwany. 2019. "Effect of Process Parameters and Electropolishing on the Surface Roughness of Interior Channels in Additively Manufactured Nickel-Titanium Shape Memory Alloy Actuators." *Additive Manufacturing* 27 (October 2018): 565–575. doi:10.1016/j.addma.2019.03.027.

Pakkanen, Jukka, Flaviana Calignano, Francesco Trevisan, Massimo Lorusso, Elisa Paola Ambrosio, Diego Manfredi, and Paolo Fino. 2016. "Study of Internal Channel Surface Roughnesses Manufactured by Selective Laser Melting in Aluminum and Titanium Alloys." *Metallurgical and Materials Transactions A* 47 (8): 3837–3844. doi:10.1007/s11661-016-3478-7.

Patterson, Albert E., Sherri L. Messimer, and Phillip A. Farrington. 2017. "Overhanging Features and the SLM/DMLS Residual Stresses Problem: Review and Future Research Need." *Technologies* 5 (4): 15. doi:10.3390/technologies5020015.

Roberts, I. A., C. J. Wang, R. Esterlein, M. Stanford, and D. J. Mynors. 2009. "A Three-Dimensional Finite Element Analysis of the Temperature Field during Laser Melting of Metal Powders in Additive Layer Manufacturing." *International Journal of Machine Tools and Manufacture* 49 (12–13): 916–923. doi:10.1016/j.ijmachtools.2009.07.004.

Shrestha, Subin, and Kevin Chou. 2018. "Computational Analysis of Thermo-Fluid Dynamics with Metallic Powder in SLM." In *CFD Modeling and Simulation in Materials Processing 2018*, edited by Laurentiu Nastac, Koulis Pericleous, Adrian S. Sabau, Lifeng Zhang, and Brian G. Thomas, 85–95. Cham, Switzerland: Springer Nature. doi:10.1007/978-3-319-72059-3_9.

Sing, S. L., and W. Y. Yeong. 2020. "Laser Powder Bed Fusion for Metal Additive Manufacturing: Perspectives on Recent Developments." *Virtual and Physical Prototyping* 15 (3): 359–370. doi:10.1080/17452759.2020.1779999.

Šmilauer, Václav, Emanuele Catalano, Bruno Chareyre, Sergei Dorofeenko, Jérôme Duriez, Nolan Dyck, Jan Eliáš, et al. 2015. *Yade Documentation*. 2nd ed. The Yade Project. doi:10.5281/zenodo.34073.

Tan, Pengfei, Fei Shen, Biao Li, and Kun Zhou. 2019. "A Thermo-Metallurgical-Mechanical Model for Selective Laser Melting of Ti6Al4V." *Materials & Design* 168 (April): 107642. doi:10.1016/j.matdes.2019.107642.

Tan, Lisa Jiaying, Wei Zhu, and Kun Zhou. 2020. "Recent Progress on Polymer Materials for Additive Manufacturing." *Advanced Functional Materials* 30 (43): 1–54. doi:10.1002/adfm.202003062.

Wang, Xiaoqing, and Kevin Chou. 2018. "Effect of Support Structures on Ti-6Al-4V Overhang Parts Fabricated by Powder Bed Fusion Electron Beam Additive Manufacturing." *Journal of Materials Processing Technology* 257 (February): 65–78. doi:10.1016/j.jmatprotec.2018.02.038.

Wang, Di, Yongqiang Yang, Ziheng Yi, and Xubin Su. 2013. "Research on the Fabricating Quality Optimization of the Overhanging Surface in SLM Process." *International Journal of Advanced Manufacturing Technology* 65 (9–12): 1471–1484. doi:10.1007/s00170-012-4271-4.

Wen, Peng, Maximilian Voshage, Lucas Jauer, Yanzhe Chen, Yu Qin, Reinhart Poprawe, and Johannes Henrich Schleifenbaum. 2018. "Laser Additive Manufacturing of Zn Metal Parts for Biodegradable Applications: Processing, Formation Quality and Mechanical Properties." *Materials and Design* 155: 36–45. doi:10.1016/j.matdes.2018.05.057.

Wu, Yu-che, Cheng-hung San, Chih-hsiang Chang, Huey-jiuan Lin, Raed Marwan, Shuhei Baba, and Weng-Sing Hwang. 2018. "Numerical Modeling of Melt-Pool Behavior in Selective Laser Melting with Random Powder Distribution and Experimental Validation." *Journal of Materials Processing Technology* 254 (November 2017): 72–78. doi:10.1016/j.jmatprotec.2017.11.032.

Yadroitsev, I., P. Krakhmalev, I. Yadroitsava, S. Johansson, and I. Smurov. 2013. "Energy Input Effect on Morphology and Microstructure of Selective Laser Melting Single Track from Metallic Powder." *Journal of Materials Processing Technology* 213 (4): 606–613. doi:10.1016/j.jmatprotec.2012.11.014.

Yu, Wenhui, Swee Leong Sing, Chee Kai Chua, and Xuelei Tian. 2019. "Influence of Re-Melting on Surface Roughness and Porosity of AlSi10Mg Parts Fabricated by Selective Laser Melting." *Journal of Alloys and Compounds* 792: 574–581. doi:10.1016/j.jallcom.2019.04.017.

Zhang, Dongyun, Pudan Zhang, Zhen Liu, Zhe Feng, Chengjie Wang, and Yanwu Guo. 2018. "Thermofluid Field of Molten Pool and Its Effects during Selective Laser Melting (SLM) of Inconel 718 Alloy." *Additive Manufacturing* 21 (100): 567–578. doi:10.1016/j.addma.2018.03.031.

Appendix A. Derivation of Eq. 5

In laser materials processing, the melt pool shape and isotherm contours are strongly dependent upon the shape of the equivalent volumetric heat source. For a Gaussian laser beam, taking into account the attenuation in the depth direction (i.e. into the powder bed and substrate) dictated by the Beer-Lambert law, the distribution of laser power density inside the material can be expressed as (Feng et al. 2017):

$$Q = I_0\alpha \cdot \exp\left(-2r^2/r_0^2\right) \cdot \exp\left(-\alpha z\right) \tag{A.1}$$

where Q, I_0, and α are the laser power density inside the material, peak laser intensity, and attenuation coefficient, respectively. We seek to define the boundaries of the 3D volume that can be approximated as an equivalent heat source in the model. To this end, the volumetric heat source is assumed to reach its boundaries when the laser power density attenuates to a certain value. This threshold boundary value of laser power density (Q_B) is equal to the value of the surface power density at a radial distance equal to the spot radius of the laser, and can be determined by:

$$Q_B = Q(r = r_0, z = 0) = I_0\alpha \cdot \exp\left(-2\right) \tag{A.2}$$

As mentioned before, the volumetric heat source is assumed to have a power density of Q_B at its bounding surface. If r_B and z_B define the locus of points that define the volumetric heat source in the cylindrical coordinate system, we have:

$$Q_B = I_0\alpha \cdot \exp\left(-2r_B^2/r_0^2\right) \cdot \exp\left(-\alpha z_B\right) \tag{A.3}$$

Combining Eqs. A.2 and A.3:

$$I_0\alpha \cdot \exp\left(-2\right) = I_0\alpha \cdot \exp\left(-2r_B^2/r_0^2\right) \cdot \exp\left(-\alpha z_B\right) \tag{A.4}$$

Simplifying Eq. A.4, we obtain:

$$2r_B^2/r_0^2 + \alpha z_B = 2 \tag{A.5}$$

Further, we note that the optical penetration depth is:

$$z_B(r = 0) = z_{PD} \tag{A.6}$$

Combining Eqs. A.5 and A.6, we obtain:

$$\alpha = 2/z_{PD} \tag{A.7}$$

Finally, combining Eqs. A.5 and A.7, we obtain:

$$r_B^2/r_0^2 + z_B/z_{PD} = 1 \tag{A.8}$$

Eq. A.8 describes an equation determining the bounding surface of the 3D volumetric heat source. In other words, the volumetric heat source is comprised of all points (r, z) such that $r \le r_B$ and $z \le z_{PD}$. This 3D shape was used as the volumetric heat source (Eq. 5) in the model, and the incident laser energy was assumed to be generated uniformly within this 3D volume.